Image-Based High-Throughput Field Phenotyping of Crop Roots[1][W][OPEN]

Alexander Bucksch[2]*, James Burridge[2], Larry M. York, Abhiram Das, Eric Nord, Joshua S. Weitz, and Jonathan P. Lynch

Schools of Biology (A.B., A.D. J.S.W.), Interactive Computing (A.B.), and Physics (J.S.W.), Georgia Institute of Technology, Atlanta, Georgia 30332; and Department of Plant Science (J.B., L.M.Y., E.N., J.P.L.) and Intercollege Graduate Degree Program in Ecology (L.M.Y.), Pennsylvania State University, University Park, Pennsylvania 16801

ORCID IDs: 0000-0002-1071-5355 (A.B.); 0000-0002-2593-3072 (E.N.); 0000-0002-3433-8312 (J.S.W.).

Current plant phenotyping technologies to characterize agriculturally relevant traits have been primarily developed for use in laboratory and/or greenhouse conditions. In the case of root architectural traits, this limits phenotyping efforts, largely, to young plants grown in specialized containers and growth media. Hence, novel approaches are required to characterize mature root systems of older plants grown under actual soil conditions in the field. Imaging methods able to address the challenges associated with characterizing mature root systems are rare due, in part, to the greater complexity of mature root systems, including the larger size, overlap, and diversity of root components. Our imaging solution combines a field-imaging protocol and algorithmic approach to analyze mature root systems grown in the field. Via two case studies, we demonstrate how image analysis can be utilized to estimate localized root traits that reliably capture heritable architectural diversity as well as environmentally induced architectural variation of both monocot and dicot plants. In the first study, we show that our algorithms and traits (including 13 novel traits inaccessible to manual estimation) can differentiate nine maize (Zea mays) genotypes 8 weeks after planting. The second study focuses on a diversity panel of 188 cowpea (Vigna unguiculata) genotypes to identify which traits are sufficient to differentiate genotypes even when comparing plants whose harvesting date differs up to 14 d. Overall, we find that automatically derived traits can increase both the speed and reproducibility of the trait estimation pipeline under field conditions.

Crop root systems represent an underexplored target for improvements as part of community efforts to ensure that global crop yields and productivity keep pace with population growth (Godfray et al., 2010; Gregory and George, 2011; Nelson et al., 2012). The challenge in improving crop root systems is that yield and productivity also depend on soil fertility, which is also a major constraint to global food production (Lynch, 2007). Hence, desired improvements to crop root systems include enhanced water use efficiency and water acquisition given the increased likelihood of drought in future climates (Intergovernmental Panel on Climate Change, 2014). Over the long term, the development of crop genotypes with improved root phenotypes requires advances in the characterization of root system architecture (RSA) and in the relationship between RSA and function.

The emerging discipline of plant phenomics aims to expand the scope, throughput, and accuracy of plant trait estimates (Furbank, 2009). In the case of plant roots, structural traits may describe RSA as geometric or topological measures of the root shape at various scales (e.g. diameters and width of the whole root system or a single branch; Lynch, 1995; Den Herder et al., 2010). These traits can be used to predict yield under specific conditions such as drought or low fertility. Understanding the diversity and development of root architectural traits is crucial, because spatial and temporal root deployment affects plant fitness, especially water and nutrient acquisition (Rich and Watt, 2013). Thus, improving plant performance may benefit from improvements in the characterization of root architecture, including understanding how trait variation arises as a function of genotype and environmental conditions (Band et al., 2012; Shi et al., 2013).

Current efforts to understand the structure of crop root systems have already led to a number of imaging solutions (Lobet et al., 2013) that are able to extract root architecture traits under various conditions (Fiorani et al., 2012), including laboratory conditions (de Dorlodot et al., 2007) in which plants are often grown in pots or glass containers (Zeng et al., 2008; Armengaud et al., 2009; Le Bot et al., 2010; Clark et al., 2011; Lobet et al., 2011; Naeem et al., 2011; Galkovskyi et al., 2012). In the case of pots, expensive magnetic resonance imaging technologies

represent one noninvasive approach to capture high-resolution details of root architecture (Schulz et al., 2013), similar to the capabilities of x-ray microcomputed tomography (μCT) systems. X-ray systems allow capturing of the root architecture at a fine scale in containers with a wide variety of soil types (Mairhofer et al., 2012; Mooney et al., 2012). It has been shown that x-ray μCT paired with specifically designed algorithms has sufficient resolution to recover the root structure in many cases (Mairhofer et al., 2013). Nevertheless, x-ray μCT systems are currently unable to image mature root systems because of technical restrictions in container size.

As an alternative, root systems can be imaged directly with a digital camera when grown in glass containers with transparent media such as gellan gum or transparent soil replacements (Downie et al., 2012). Such in situ imaging benefits from controlled lightning conditions during image acquisition, even more so when focusing on less complex root structures of younger plants that allow three-dimensional reconstruction (Clark et al., 2011; Topp et al., 2013). Under such controlled conditions, it is expected that imaging would enable the study of growth of roots over time (Spalding and Miller, 2013; Sozzani et al., 2014).

However, all of the above-listed solutions have been used primarily to assess root structures in the early seedling stage (French et al., 2009; Brooks et al., 2010; Sozzani et al., 2014) to approximately 10 d after germination (Clark et al., 2011), which makes it all but impossible to directly observe mature root systems. For example, primary and seminal roots make up the major portion of the seedling root system in maize (*Zea mays*) during the first weeks after germination. Later in development, postembryonic shoot-borne roots become the major component of the maize root system (Hochholdinger, 2009), not yet accessible to laboratory phenotyping platforms. In addition to phenological limitations, current phenotyping approaches for root architecture require specialized growth conditions with aerial and soil environments that differ from field conditions; the effects of such differences on RSA are only sparsely reported in literature (Hargreaves et al., 2009; Wojciechowski et al., 2009).

Indeed, high-throughput field phenotyping can be seen as a new frontier for crop improvement (Araus and Cairns, 2014) because imaging a mature root system under realistic field conditions poses unique challenges and opportunities (Gregory et al., 2009; Zhu et al., 2011; Pieruschka and Poorter, 2012). Challenges are intrinsic to roots grown in the field because the in situ belowground imaging systems to date are unable to capture fine root systems. As a consequence, initial attempts to characterize root systems in the field focused on the manual extraction of structural properties. Manual approaches analyzed the root system's branching hierarchy in relation to root length and rooting depth (Fitter, 1991). In the late 1980s, imaging techniques were first used (Tatsumi et al., 1989) to estimate the space-filling behavior of roots, an estimation process that was recently automated (Zhong et al., 2009). A weakness of such approaches is that exact space-filling properties, such as the fractal dimension, are sensitive to the incompleteness of the excavated root network (Nielsen et al., 1997, 1999). In particular, the box counting method was criticized for above-ground branching networks of tree crowns (Da Silva et al., 2006). The same critiques apply to root systems, because fine secondary or tertiary roots can be lost or cutoff or can adhere to each other during the cleaning process, making it impossible to analyze the entire network.

As an alternative, the shovelomics field protocol has been proposed to characterize the root architecture of maize under field conditions (Trachsel et al., 2011). In shovelomics, the researcher excavates the root at a radius of 20 cm around the hypocotyl and 20 cm below the soil surface. This standardized process captures the majority of the root system biomass within the excavation area. After excavation, the shoot is separated from the root 20 cm above the soil level and washed in water containing mild detergent to remove soil. The current procedure places the washed root on a phenotyping board consisting of a large protractor to measure dominant root angles with the soil level at depth intervals and marks to score length and density classes of lateral roots. A digital caliper is used to measure root stem diameters (Fig. 1). Observed traits vary slightly from crop to crop but generally fit into the following categories by depth or root class: angle, number, density, and diameter. In this way, field-based shovelomics allows the researcher to visually quantify the excavated structure of the root crown and compare genotypes via a common set of traits that do not depend on knowledge or observation of the entire root system network. Of note, shovelomics is of particular use in developing countries, which have limited access to molecular breeding platforms (Delannay et al., 2012), and for which direct phenotypic selection is an attractive option.

Nonetheless, direct phenotypic selection for root traits of field-grown root systems comes with a number of caveats and drawbacks. To date, the quantification of mature root systems is highly dependent on the researcher, reducing the repeatability of measured quantities (Gil et al., 2007). In addition, manual approaches impose limitations on both the number of accessible traits and the number of samples collected. For example, a typical shovelomics phenotyper can gather 10 to 12 traits from a sample in 2 min or approximately 200 samples in a typical workday (Trachsel et al., 2011). This means that evaluating a statistically more significant trial of 1,000 samples may take 5 d or more. Such a time span introduces variation owing to plant growth and phenology. On the other hand, shovelomics is adaptable to both monocot and dicot roots; therefore, its procedure can be scaled over the huge variety of root morphologies in dicots and monocots. For these reasons, we contend that shovelomics represents a valued target for an automated high-throughput phenotyping approach in the field.

We introduce an imaging approach for high-throughput phenotyping of mature root systems under realistic soil conditions to address the limitations of manual data collection (Fig. 2, I and II). Our new algorithms directly

Figure 1. A, Classic shovelomics scoring board to score the angle of maize roots with the soil tissue. B, An example to score rooting depth and angle in common bean.
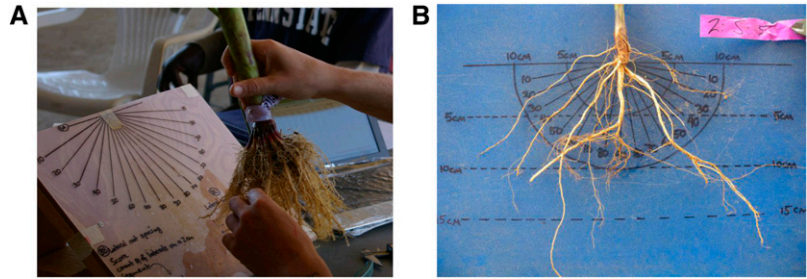

extract root architecture traits from excavated root images (Fig. 2, III and IV). Rapid imaging of the roots and decoupled analysis of the collected data at a later time improve both the throughput and synchronization of experiments. In addition to traits that are developed from shovelomics, our algorithms extract previously inaccessible traits such as root tip diameter, spatial distribution, and root tissue angle (RTA). Overall, our approach allows imaging directly at field sites with an easily reproducible imaging setup and involves no transportation cost or expensive hardware. We demonstrate the utility of our approach in the field-based analysis of maize and cowpea (*Vigna unguiculata*) architecture.

RESULTS

Low-Cost, Reproducible, and Field-Based Protocol for Imaging Plant Roots

We extend the manual trait estimation procedures described in shovelomics (Trachsel et al., 2011) in order to facilitate estimation of root traits based on digital images taken under field conditions. Similar to shovelomics, the root crown is excavated, washed in water, and then placed on a board to estimate root traits. Image-based estimation of root traits requires improvements in the contrast between root and board object segmentation on the board and automated labeling. To address these challenges, we developed a new imaging board and

Figure 2. I, Imaging board on the example of a maize root. The experiment tag is used to capture an experiment number, and the scale marker allows the correction of camera tilting and transforming image coordinates into metric units. II, Camera mounted on a tripod placed on top of the imaging board coated with blackboard paint. Note that images were taken with protection against direct sunlight not shown in the image. III, Example of the segmentation of the original image into a binary image and then into a series of image masks that serve as input to estimate traits for monocot and dicot roots. The sample is that of a maize root, 40 d after planting at the URBC. IV, The imaging pipeline for dicot roots and sparse monocot roots: Original image on the imaging board (a), derived distance map where the lighter gray level represents a larger diameter of the imaged object (b), medial axis includes loops (c), and loop RTP with a sample of the root branching structure (d). Colors are randomly assigned to each path. The sample is that of a cowpea root, approximately 30 d after planting at the URBC.
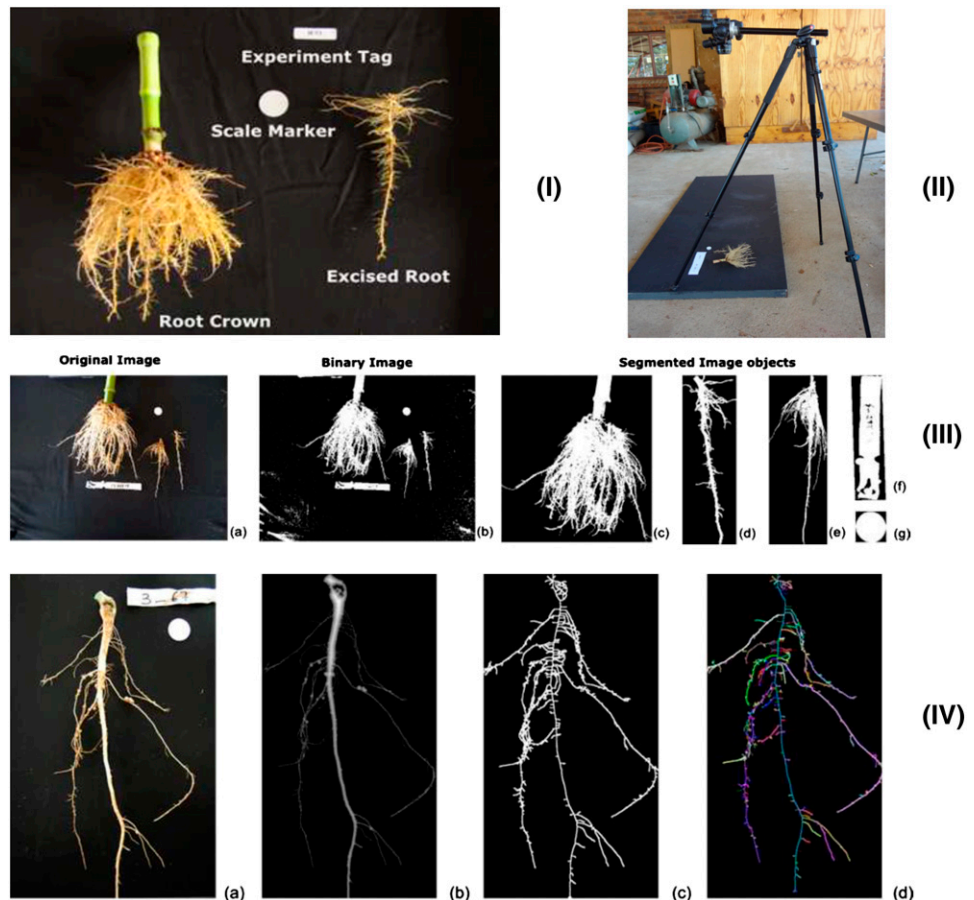
imaging protocol. The new imaging board consists of a black background with diffuse reflectance properties on which a circle of known diameter is freely positioned, which enables calculation of units (Fig. 2I; "Materials and Methods"). Next, images of the root system were photographed using a digital camera mounted on a tripod (Fig. 2II; "Materials and Methods"). Finally, we developed an automated pipeline to derive measurements from the root crown and the excised root samples. In the first step, the objects on the imaging board are detected and segmented into individual image masks. Each individual mask represents the root crown, excised root sample, experimental tag, and scale marker (Fig. 2III). As a precursor to trait estimation, the algorithm automatically detects the marker and tag using geometric priors; the geometry of the marker is then used to automatically calibrate the trait measurements. In the second step, a structural description of the root crown and the excised root is computed. The structural description, called the root-tip path (RTP), is a curve representation that samples the root architecture (Fig. 2IV). The sampling is necessary because the actual root networks of mature root systems occlude its interior, and smaller roots may bind together when the roots are excavated and washed. Finally, we utilize the image masks and RTP to estimate architectural traits of dicot and sparse monocot root system based on angle, diameter, length, width, and density measures ("Materials and Methods").

The Digital Image Analysis Pipeline Enables Field-Based Estimation of Root Traits

All trait measurements rely on the computation of root length, diameters, branching angles, density, and spatial root distribution estimations. These measurements, whose distributions are summarized in trait values, characterize the root architecture. Technically, traits are distinguished based on whether they are computed from (1) the image mask, (2) the RTP skeleton (Fig. 2IV; "Materials and Methods"), or (3) the excised root component. The image mask (Fig. 2IIIc) enables estimation of the root-width profile as well as root density. The RTP skeleton is a loop-free sampling of the medial axis derived from the root shape visible in the image. The RTPs describe significant root parts by the number of paths passing through the same location in the image determined on the basis of detectable tips in the image.

As a consequence, the RTP skeleton allows the calculation of the length of significant root parts, the radius at each location as the distance to one of the at least two closest pixels on the root mask boundary, branching frequencies, and path length from the distance between branching points and angles between a root part emerging from the tissue of a parent root. Our segmentation of the original images enables separate analysis of an excised crown root (Fig. 2, IIId and IIIe). The intermediate mask images used in our pipeline allow a user to visually identify possible miscalculations due to substandard imaging conditions. Tables I and II summarize all currently computed traits.

We determined the technical error of our pipeline with five persons that were untrained in the imaging protocol ("Materials and Methods"). We used a black block with a cylindrical groove to hold the maize root crown and increase the repeatability of the placement. We additionally placed a bean root without the groove to demonstrate the concept of the RTA compared with the soil tissue angle (STA). For maize, we obtained relative SDs below 10% except for average root density, diameter at 90% depth, and the spatial root distribution in X. The majority of traits such as D and DS values ("Materials and Methods") showed relative SDs below 5.0%. For the freely placed bean, we found that the RTA measurements are more robust to placement errors than the STA measurements. The median RTA resulted in an average residual of 3.0°, which corresponds to a relative SD of 5.2%. By contrast, the median STA showed an average residual of 9.4° corresponding to a relative SD of 22.7%. The maximal width measurements resulted in a relative SD less than 1% in maize, but 7.0% in bean depending on root placement. Overall, in both cases, our test showed the expected robustness of our traits to translational and rotational differences in the placement of the root. Nevertheless, we suggest the use of tools to guide the root placement to further improve the collected data quality. The full test results are available in the Supplemental Data Sets S9 and S10.

Validation of Image-Based Traits

We validated the diameter traits, which were derived with a caliper in the field on 1,445 cowpea roots representing 188 genotypes. Figure 3 shows the correlation of taproot diameters (see Supplemental Fig. S25 for dicot nomenclature) at two depth levels derived as field measurements (Fig. 3A), the direct comparison between manually and image-based derived diameters (Fig. 3B), and image-based measurements at two depth levels (Fig. 3C). All three comparisons yield similar Pearson correlations of 0.49 ± 0.02 with $P < 0.001$. The conceptual difference between field- and image-based measurement is that manually measured diameters are taken at a certain depth below the soil line, not accounting for differences in plant age. Continuing growth induces errors emerging from simultaneous lateral thickening and elongation in depth. By contrast, the image-based measurement is taken as a certain percentage of the maximal depth to compensate for differences in plant age, assuming a linear scaling of length and thickness within the given time frame. In addition, we found strong correlations between image-based and field-measured traits, which were not accessible in the image. For example, the number of third-order roots scored in the field was correlated with a strong Pearson $r = 0.8$ to the number of detectable RTPs as shown in Figure 3. Because RTPs are derived from the number of tips visible in the image, the Pearson $r = 0.8$ is explained by the exponentially growing amount of branches. Furthermore, the RTPs are correlated with the nodulation score for the cowpea data set ($r = 0.59$), which again is explained

Table I. *Overview of crown traits derived for the root stock*

N/A, Not available.

Name	Definition	Closest Trait Analog in Shovelomics
Average root density	Ratio between foreground and background pixels of the extracted root	Scoring of density
STA X	Angle between an RTP at x% length and the x axis calculated as ar$ctan$ (m), where m is the slope of the fit line	Shovelomics angle at certain depth for dicots
Dominant STA 1 and 2	Average of the first and second significant peak in the in the histogram of calculated solid tissue angles binned in 10° steps	Shovelomics angle for dicots
Min/median/max STA	Minimal, median, and maximal of all calculated STAs	N/A
Dominant RTA 1 and 2	Average of the first and second significant peak in the histogram of calculated RTAs binned in 10° steps	N/A
Min/median/max RTA	Minimal, median, and maximal of all calculated RTAs	N/A
Median/max width	Median/maximum of the calculated width in the width height diagram	Only max width or selected representative width
D10 to D90	Accumulated width over the depth at x%. The change in width accumulation denotes a change of the root-top angle	N/A, but closely related to the root-top angle for maize
DS10 to DS90	Slope of the graph of D values	N/A
Spatial root distribution (as separate X and Y components)	Displacement of the center of mass between the bounding box of the RTP skeleton and the RTP skeleton excluding the central path	N/A
Stem diameter	Diameter at the beginning of the root top. We use the first branching point of the filtered medial axis as a characteristic diameter	Caliper measurement
Central path diameter X	The diameter at x% length of the central path	Diameter at a defined depth below the soil line
Max diameter at 90% depth	Maximal tip diameter in the last 10% of the image	Measured for dicots
Tip diameter distribution	Exponent of the exponential function fitted through the tip diameter histogram	N/A
Median/mean tip diameter	Median and mean tip diameters of all tips	N/A

by the exponentially growing amount of branches with increasing hierarchies allowing more nodulation.

In addition to the correlations found for cowpea, we found strong correlations for nine available maize genotypes (Fig. 4). Measurements of manually scored lateral root length and image-based estimated lateral root length of the brace root resulted in a Spearman ($P = 0.0367$). Together with the caliper and image-based measurements of stem diameters (Spearman $r = 0.83$, $P = 0.0053$), the measurements validated our image-based measurement pipeline (Supplemental Figs. S1 and S2). As expected, the crown and brace root angles were correlated with the D10 trait (Supplemental Figs. S3 and S4) and yielded significant Spearman $r = -0.82$ and $r = -0.69$ ($P = 0.0072$ and $P = 0.0379$), respectively. The negative correlations are explained with the geometric constraint that the steeper

the root angles to the soil line are, the less width is accumulated at the D10 level. The surprising result in maize is the opposite correlation of the number of crown and brace roots at the D20 to D60 values. For example, the D20 value resulted in a negative Spearman $r = -0.73$ ($P = 0.0379$) with the manually counted number of brace roots. By contrast, the D20 value and the number of crown roots significantly correlated with a positive Spearman $r = 0.88$ and a significance value of $P = 0.0018$ (Supplemental Figs. S5 and S6). Under the assumption that crown roots maximize in number within the available volume enclosed by brace roots, the correlation is then positive because increasing width accumulation yields more crown roots at the given depth range. We conjecture that width accumulation of crown roots increases with an increasing number of crown roots and leads to shallower root angles because larger

Table II. *Overview of traits computed for the excised root sample*

| Name	Definition	Closest Trait Analog in Shovelomics
Nodal root length	Length of the central path along the excised root	Scored from representative sample
Average nodal root diameter	Average root diameter along the central path of the excised root	N/A
Distance to first lateral	Path length from the top pixel of the excised root to the first detected emerging lateral of the filtered medial axis	Distance to first lateral as score
Lateral branching frequency	Estimate of the lateral branching frequency calculated as: (number of laterals)/(nodal root path length)	Density scores
Average lateral length	Average length of the detected lateral roots emerging from the central path long the excised roots	Length score
Lateral min/mean/max RTA	Minimal/mean/maximal angle of detected laterals emerging from the central path along the excised root	N/A
Median/mean lateral diameter	Median/mean of all lateral tip diameters	N/A
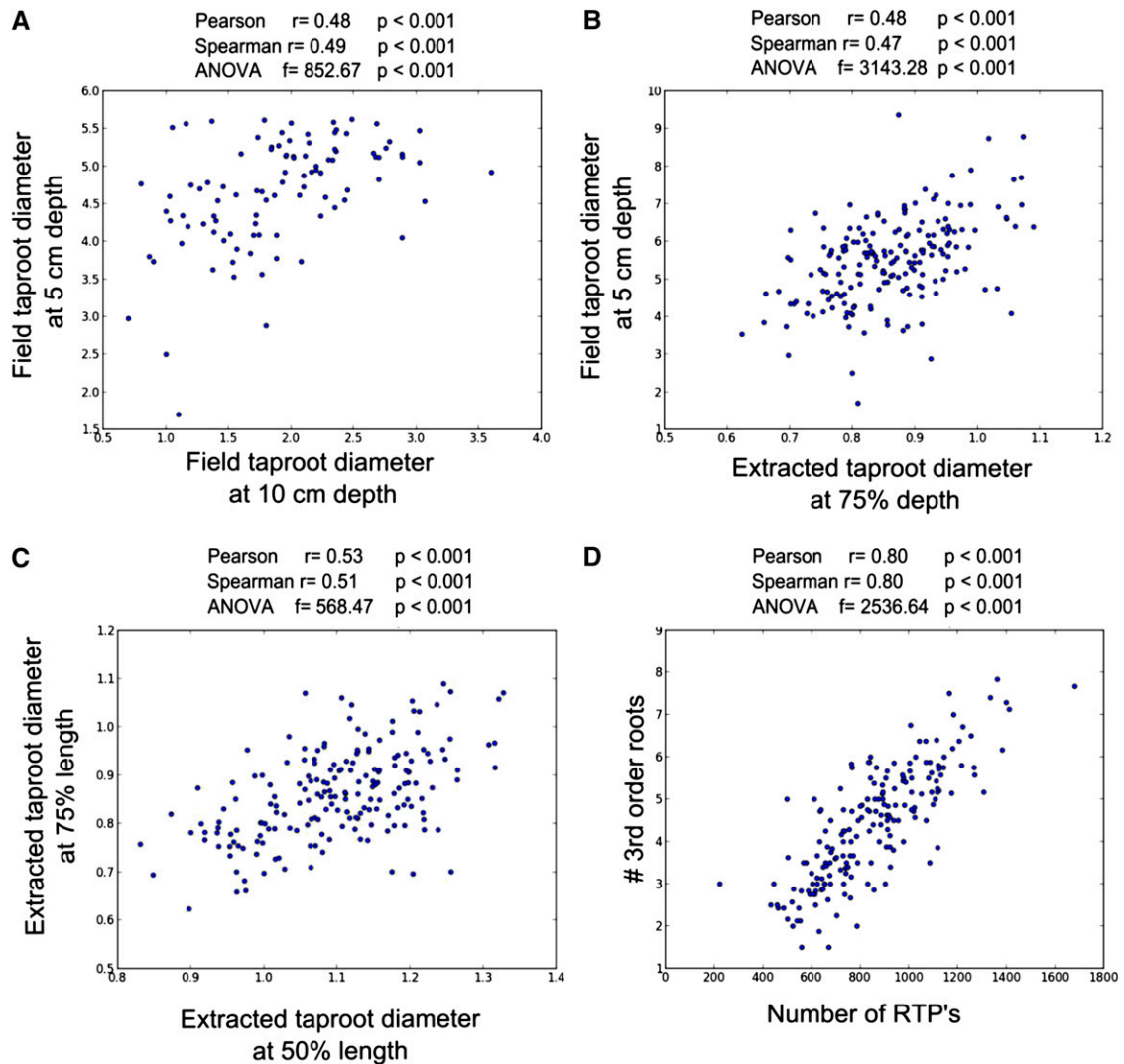
Figure 3. Trait correlations in cowpea. A, Results from field measurements of taproot diameters at 5- and 10-cm depth show correlations close to $r = 0.5$ for Spearman and Pearson coefficients. Note that not all plants reached 10-cm depth. B, An example of confirming results with $r = 0.5$ for Spearman and Pearson coefficients was achieved in correlation between the field-measured 5-cm depth level and the diameters at 75% of the central path length. C, The central path diameters extracted from images are shown with similar correlation coefficients than observed with manual field measurements. D, A surprising correlation: The number of third order basal roots in cowpea is highly correlated with the overall number of RTPs. Both correlation measures together (Spearman r and Pearson r) suggest even linear dependency. The ANOVA analysis confirms that both measurements are taken from different quantities for both correlations. All diameter measurements are in millimeters and data points represent averages per genotype.

initial width accumulation is associated with shallower root angles for brace and crown roots (see above for D10 analysis and Supplemental Fig. S24 for nomenclature). Additional analysis on the level of individual plants can be found in Supplemental Figures S31 to S36. The correlations to manual measured traits have known or hypothetical importance in soil resource acquisition (Lynch, 2011 and Lynch, 2013).

Image-Based Traits Exhibit High Differentiation Potential

We selected nine maize genotypes for diversity in lateral root density, nodal root angle, and nodal root number (see Fig. 4 for examples). In the following, we characterize the maize data set by comparing relative phenotypic variation (RPV) as estimated using shovelomics and image-based traits. The RPV of a trait for a given data set is heuristic, defined as the ratio between the variance V_d of the trait of all roots of the data set and the average trait variance per genotype V_{avg} as follows:

$$\text{RPV} = \frac{V_d}{V_{avg}}$$

Traits are more likely to be useful in differentiating genotypes when their RPV is significantly greater than 1.

Figure 4. Examples of maize genotypes selection from the Wisconsin diversity panel. The figure shows increasing root system width and shovelomics angle from left to right. The top row shows the complete root crown, and the bottom row shows the root crown with brace roots removed to reveal the crown roots. All six images show a selected representative nodal root at the right of the root crown.

An RPV of approximately 1 indicates that a given phenotypic trait is similarly distributed over given genotypes. In Figure 5, we show the RPV values of all traits for the maize crown roots. Manual measurements of the rootstock yielded only the stem diameter with an RPV above 2.5. By contrast, the absolute image-based measurements such as root density, median/maximum width, and spatial root distribution show RPV values above 2.5, suggesting differentiation between phenotypes in the given data set. Note that the stem diameter estimated from the images shows lower RPVs than the manually derived stem diameter. The difference in the RPV for the stem diameter is a consequence of the visual choice of a representative measurement location by the phenotyper. By contrast, the relative measurements of D and DS values show often greater RPVs than the comparable crown root angle measured in the field.

The RPV of the excised root sample traits reveals differences in the measurement methodology. Whereas a field phenotyper scores the average lateral length on a scale from 0 to 9 (RPV > 3.5), the length of the RTPs is determined in centimeters with an RPV close to 1. This effect can be explained by a binning effect induced by the scoring scheme of the researcher, that does not reflect the variation in length (compare visually Fig. 4). By contrast, we observed an RPV > 2 from images for the brace root (Supplemental Fig. 11). Similarly to the RPV value, we obtain the broad sense heritability (H^2) from our trait data (Einspahr et al., 1963).

$$H^2 = \frac{V_d}{V_{avg} + V_d}$$

The crown root traits resulted in $0.55 < H^2 \leq 0.81$ for traits measured manually and $0.56 < H^2 \leq 0.83$ from images (Supplemental Fig. S12). The largest H^2 was obtained for the lateral density (top) in the case of the manual measurements and for the median width and D10 in the case of the image-based measurement. For the brace root traits, we observed $0.66 < H^2 \leq 0.85$ for traits measured manually and $0.56 < H^2 \leq 0.80$

Figure 5. RPV analysis of the crown root measurements. Traits are more likely to be useful in differentiating genotypes when their RPV is significantly greater than 1 (blue line). Trait definitions are found in Tables I and II. TD, Tip diameter.
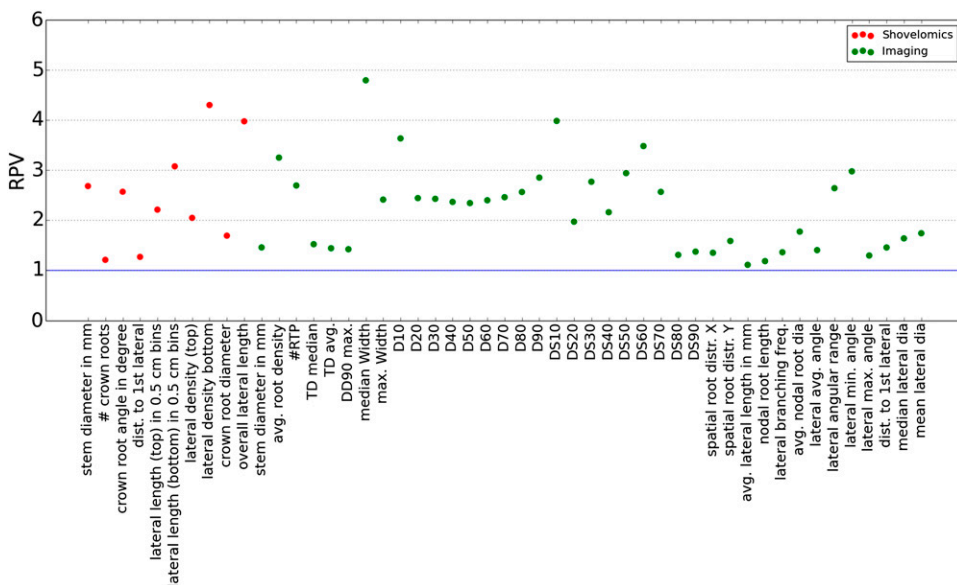
from images (Supplemental Fig. S13). The most heritable traits were lateral length (bottom) for the manual measurements and average root density for the image-based measurement. Note here that the heritability measure often results in a similar trait ranking than the RPV value, but does not reflect the strength of genotype differentiation.

We demonstrate the intergenotype versus the intragenotype variability for the crown root traits obtained with our imaging algorithms in Figure 6 and the manually derived traits in Figure 7. In both figures, we highlight the genotypes OH43, 4226, and B103 for direct comparison. Here we derived the normalized mean values as the robust sample mean from the z-score values within the three-sigma interval (Maronna et al., 2006). The associated SEs (of the mean, shown as error bars) in both figures give insight into the precision of the population mean. Nonoverlapping error bars visualize that the three example genotypes can be distinguished by the mean of a subset of traits. Pairwise comparison of genotypes per trait reveals that each genotype is distinguishable by at least eight image-based traits and one manually measured trait (Figs. 6 and 7, bottom). Most notably, we observed improved distinction for the distance to the first lateral for the image-based traits. Although field practice assigns a researcher-dependent distance score showing no variation between eight of the chosen genotypes, the image-based measurement still distinguishes different distances. The comparison of root angle measurement in the field and D and DS values that describe the cumulative width over the depth shows that distinctions between genotypes can be made with both the absolute angle measurement in the field and the D and DS values derived from the images. Supplemental

Figures S7 to S10 and S14 to S17 contain the intragenotype variation and full-resolution figures for brace and crown root images (see Supplemental Data Sets S6 to S8).

Differentiating Genotypes in Massive Diversity Panels

We evaluated image-based traits on a cowpea diversity panel consisting of 188 genotypes (see Fig. 8 for examples). Such large diversity panels pose a trade-off between two additional problems. First, long harvesting times introduce phenological effects requiring robustness to varying plant age in the trait definition. In our example, the harvesting duration was 14 d. Second, The large amount of genotypes requires high sensitivity of the traits to extract and differentiate the phenotypes present in the data set. In our cowpea study, comparable differentiation of phenotypes with diameters measured in the field and in images was achieved. Overall, the RPV values of the cowpea study are lower (<2.4) than the RPV values of the maize study (up to 7 for the brace root and up to 4.5 for the crown root; Fig. 9). Lower RPV values can be explained with the far larger amount of genotypes (188 for cowpea versus 9 for maize), constituting a full diversity panel. Directly comparable measurements such as the stem diameter resulted in similar RPV values about 1.6 and the correlated traits number of RTP paths and third-order roots are similarly strong at around 1.9. The diameter measurements of tap root and comparable central path diameter show similar differentiation potential in their RPV values. Central path diameter at a fraction of the maximal depth is in the range between 1.3 and 1.4, which is in alignment with the RTP values of the taproot diameter at 5- and 10-cm depth. The taproot diameter at 15-cm
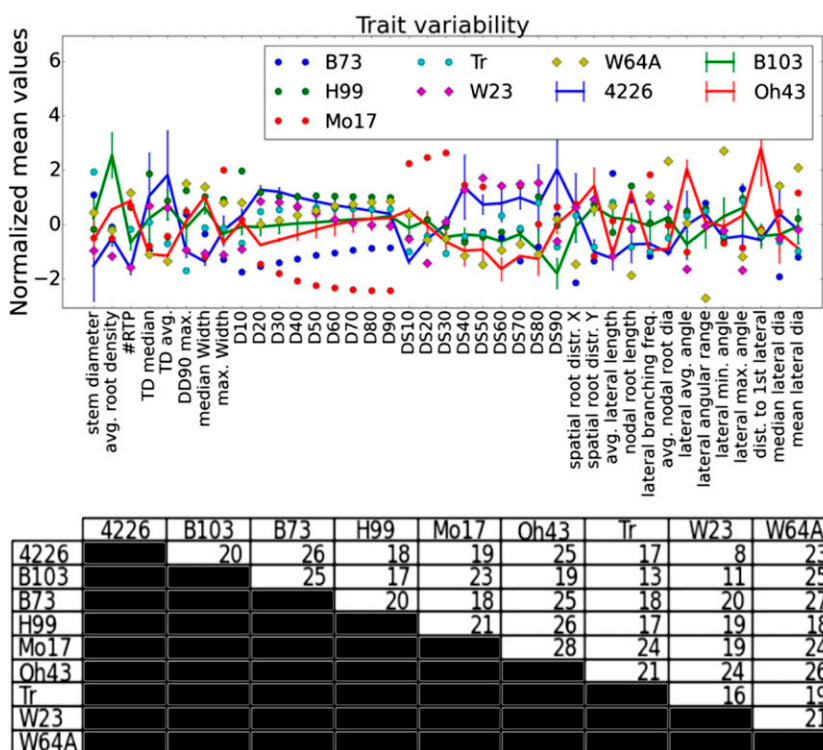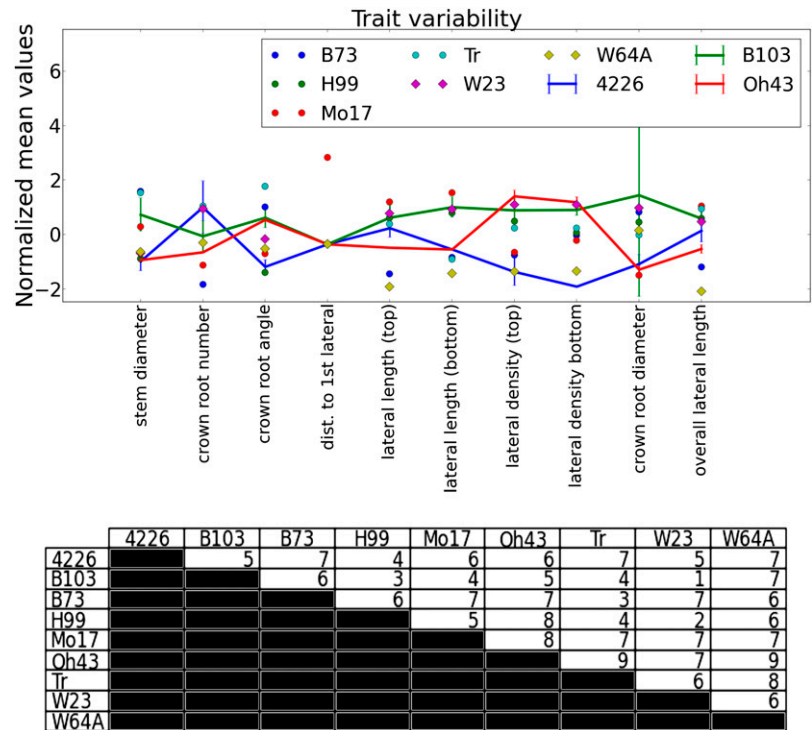

Figure 6. Top, Image-based phenotype differentiation. Normalized mean trait values of traits derived from crown root images. The intergenotype variation for the crown roots of the nine examined maize genotypes is shown. The points represent average normalized values. The connection between points allows the reader to visually identify the three genotypes shown in Figure 4. The error bars indicate the SEM. Note that relative traits only differentiate at certain depth levels. Bottom, The number of traits that distinguish a pair of genotypes in the maize study. For each combination, at least eight distinguishing traits were found. DD90max, Maximum diameter at 90% to 100% depth; TD, tip diameter.

	4226	B103	B73	H99	Mo17	Oh43	Tr	W23	W64A
4226		20	26	18	19	25	17	8	23
B103			25	17	23	19	13	11	25
B73				20	18	25	18	20	27
H99					21	26	17	19	18
Mo17						28	24	19	24
Oh43							21	24	26
Tr								16	19
W23									21
W64A									

Figure 7. Top, Phenotype differentiation with shovelomics. Normalized mean trait values show the intergenotype variation for the crown roots of the nine examined maize genotypes. The points represent average normalized values. The connection between points allows the reader to visually identify the three genotypes shown in Figure 4. All density and distance measures are researcher scores. Bottom, The number of traits that distinguish a pair of genotypes in the maize study. For each combination, at least one distinguishing trait was found.

	4226	B103	B73	H99	Mo17	Oh43	Tr	W23	W64A
4226		5	7	4	6	6	7	5	7
B103			6	3	4	5	4	1	7
B73				6	7	7	3	7	6
H99					5	8	4	2	6
Mo17						8	7	7	7
Oh43							9	7	9
Tr								6	8
W23									6
W64A									

depth is the trait with the strongest RPV value. However, only about 30% of all measured roots reached a taproot length of 15 cm, which suggests that the RPV value is artificially high and the actual presence of a 15 cm-deep taproot might constitute a novel trait. Similarly, we observed stronger differentiation for all second dominant angles (RPV > 2.5) obtained with the image-based trait estimation. A second dominant angle is not obtained for all genotypes, which again suggests that the presence of such an angle might constitute a novel trait. The second dominant RTA showed the strongest differentiation potential with RPV = 3.2. Mean and maximum width differentiated with an RPV value around 1.5, similar to the related measures of basal and adventitious root angles, whereas D and DS values performed less strong

(RPV < 1.4) compared with the maize study. The broad sense heritability (Einspahr et al., 1963) peaked at H^2 = 0.76 for the manual cowpea traits (nodulation score) and at H^2 = 0.65 for the image-based traits (number of RTPs). Notably, these are two strongly correlated traits, as shown in Figure 3D. The taproot diameter at 15-cm depth and the number of first order laterals at 15-cm depth below the soil line show a strong H^2. We considered these two heritability measures as unreliable, because only a few roots reached 15-cm depth or length. The heritability for all cowpea traits is shown in Supplemental Figure S20.

The absolute trait of the second dominant angle distinguished genotypes with large angular differences as shown in the example in Figure 10. The large SE for the first dominant angle possibly emerges from the

Figure 8. Six examples from the cowpea diversity panel. Different root architectures in mature cowpea with the genotype denoted in each image are illustrated.
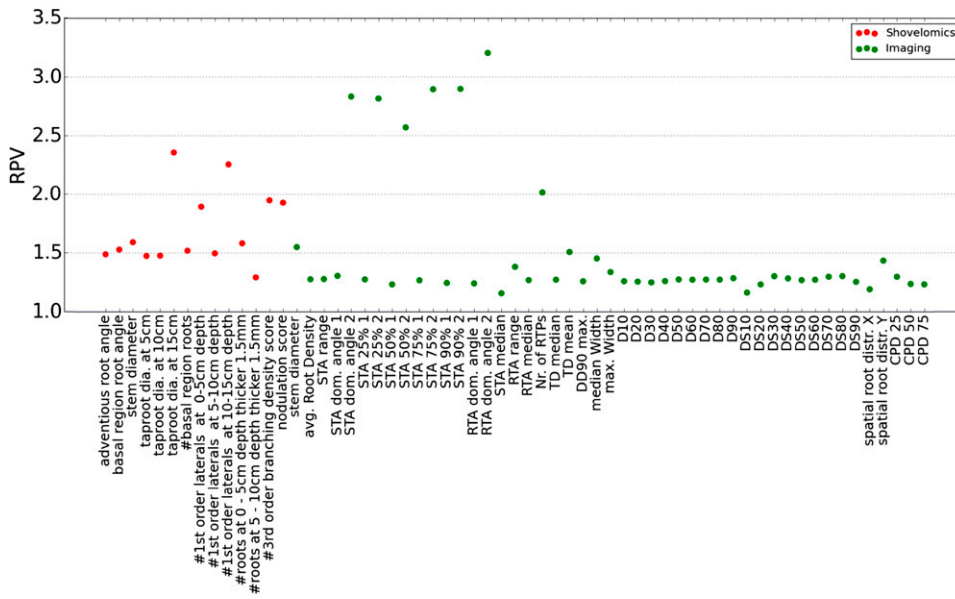
Figure 9. RPVs of shovelomics and image-based traits for the cowpea diversity panel. Traits are more likely to be useful in differentiating genotypes when their RPV is significantly greater than 1. Note that the manual traits counting first order laterals do not include counts in the basal region of the root. All field scores ranged from 0 (low) to 9 (high). The figure is comparable to Supplemental Fig. S30 showing RPVs for GIA Root traits.

difference in root age and is also observable in the angles of the field measurement (Supplemental Fig. S22). In the selected examples in Figure 8, D and DS values again distinguish the genotypes by means of the SE. Nevertheless, on the large diversity panel, we found that there exists no single trait to distinguish all genotypes. In our example study, we found that all 188 cowpea genotypes could be distinguished by at least one image-based trait, whereas five genotypes could not be distinguished with the manual field measurement. We predominately found that D and

DS values and diameter measurements of the stem and along the central path are most suited to distinguish genotypes. The D and DS values differentiate cowpea phenotypes better than corresponding angle measurements collected by the field researcher, because the traits are derived relative to the maximum depth of an individual root. Thus, the difference in plant age is less, influencing the actual measurement. Large versions of the figures, the corresponding data sets, the intragenotype variation (Supplemental Figs. S18–S22), and the pairwise
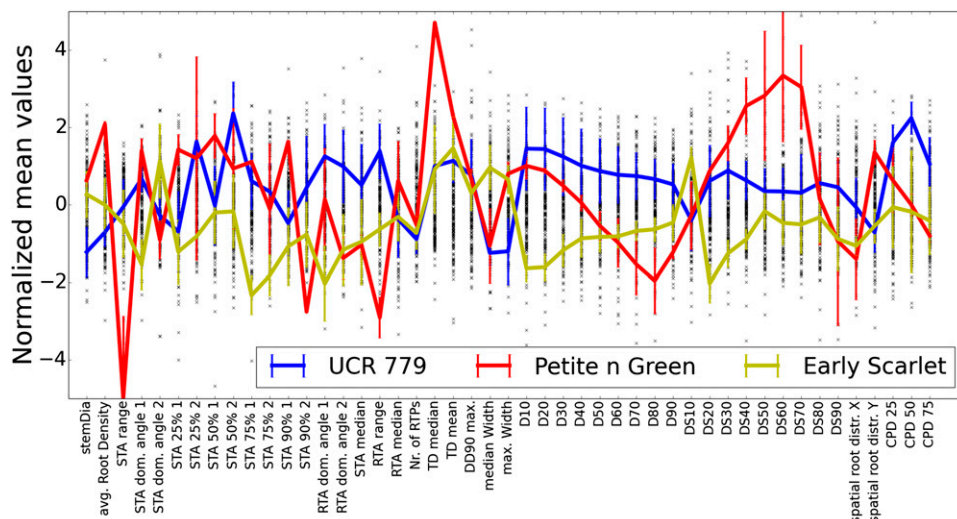

Figure 10. Overall phenotype differentiation of the cowpea diversity panel. Black crosses show the trait values of the whole data set, and the lines are three selected examples with error bars denoting the SEM. The three example genotypes distinguish by at least one D and DS value and by the second dominant angle. The D values demonstrate that UCR 779 differentiates from Petite n Green at higher depth levels and from Early Scarlet at deeper depth levels. UCR 779 differentiates additionally in central path diameters from Petite n Green and Early Scarlet. The connection between points allows the reader to visually identify the three of the six genotypes shown in Figure 8. DD90max, Maximum diameter at 90% to 100% depth; dia., diameter; TD, tip diameter; CPD, central path diameter.

comparison matrices can be found in Supplemental Data Sets S1 to S3.

CONCLUSION AND FUTURE DIRECTIONS

We have developed image-processing algorithms in alignment with the needs of current field-research practice to estimate root phenotypes in real soil conditions. In doing so, we have (1) developed a low-cost, reproducible protocol for image-based root analysis; (2) developed imaging processing methods to automatically classify multiple root components (and experimental tags) from a single image; (3) developed a novel set of localized root system traits based on the principle of RTPs; and (4) demonstrated that these traits can differentiate among genotypes of both cowpea and maize. In contrast with algorithms available in existing software packages such as RootNav (Pound et al., 2013), SmartRoot (Lobet et al., 2011), or DART (Le Bot et al., 2010), which focus on the detailed measurement of an individual root system by a user, our algorithms allow the automatic extraction of many root traits in a high-throughput fashion. Naturally, our approach comes at the cost of a greater dependency on image quality and a larger amount of root samples to achieve significant average trait values. However, semiautomatic approaches are equally dependent on the visibility of root tips in images.

Overall, we found that angular, diameter, width, and length measurements derived from images show similar or in some cases superior RPV and differentiation in terms of the SEM compared with manual shovelomics quantification. In our example studies, we showed that image analysis is an attractive alternative to extract crop root architecture traits also under field conditions. In addition, we identified a subset of traits (central path diameter, as well as D and DS values) that have the potential to analyze large field studies with long harvesting durations. We hope that our algorithms enable large-scale plasticity studies on roots in the field because we see high-throughput plant phenotyping under field conditions as enabled by our approach.

We developed RTPs as a representation of significant root parts, from which additional information can be computed. Nevertheless, our approach has shown that new conclusions can be drawn from the computed data, because of increased trait robustness and measurement resolution. In addition, we provide 13 traits previously not accessible in the field such as tip diameter, symmetry measures, or RTA, which enriches the set of traits to be used by field researchers. The underlying assumptions for the RTPs allow us to objectively simulate the scoring and measurement of field researchers. Our traits include localized diameter, angle, length, or width measurements at certain depth levels of major root components. In that
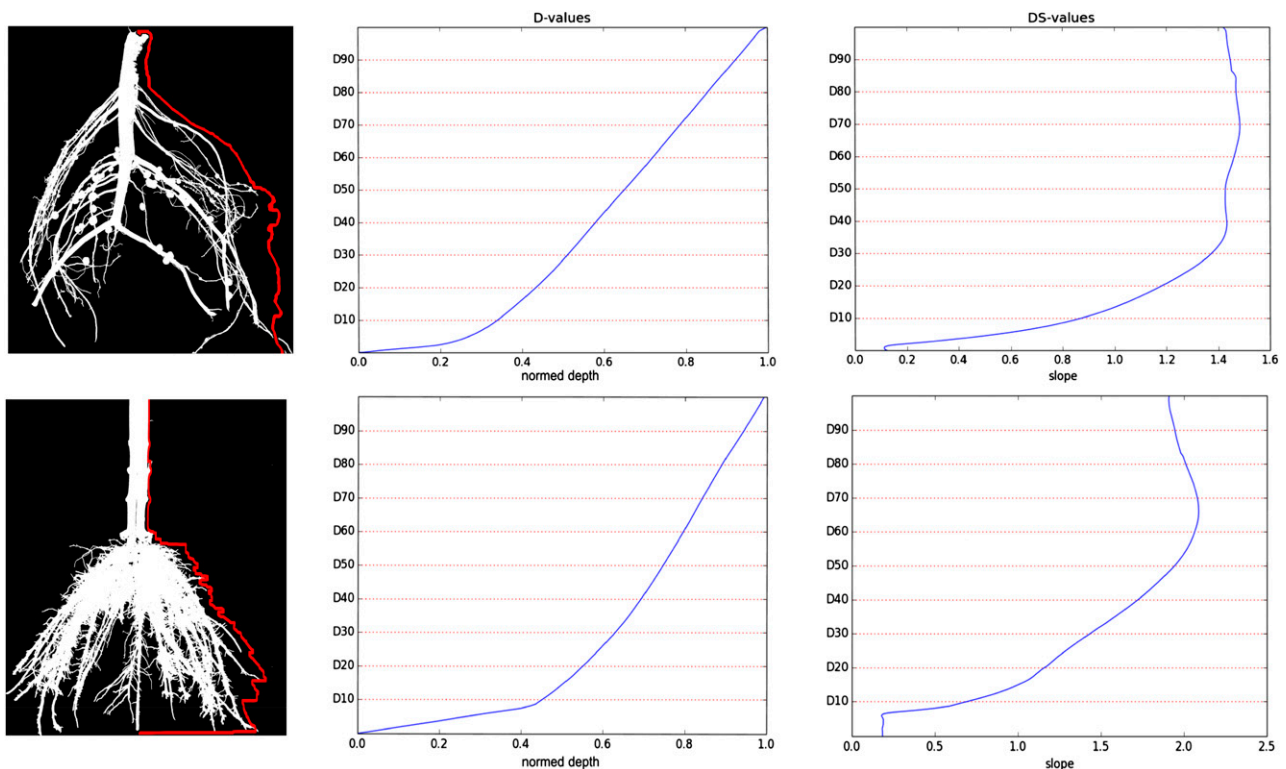

Figure 11. Image masks overlaid with the width profile (red) and the corresponding cumulative width and slope function from which the D and DS values are calculated. Top, Cowpea root. Bottom, Maize root. Note that the width profile does not have to match the outline of the root, because the outline is not always symmetric to a vertical and straight line. It is also visible in the cumulative curve that the D values are robust to single roots sticking out of the crown.

Input: *MA* = **[size of original image]** //Medial axis as 2D array with weights derived from the distance field,

      RootTop = (row,column) //a pair of values denoting the location of the RootTop on MA

Output: *RTPImage*

RTP= [[(row,column)]]   //array of arrays of locations (pair of values) on MA

RTPImage = [size of MA] //2D array initialized with zeros

 # Computing Root-Tip-Paths

For each *tip* **in** *MA* **do:**

      compute *shortest path* **to** *RootTop*

      append *shortest path* **to** *RTP*

 # Building a loop free hierarchy

For each *path* **in** *RTP*:

      For each *(row,column)* **in** *path*:

            Increment *RTPImage[(row,column)]* **by 1**

return *RTPImage*

Figure 12. Principle of the RTP algorithm as pseudocode.

sense, our algorithms are complementary to approaches such as GiA Roots (Galkovskyi et al., 2012) that predominantly focus on global root traits. In addition to global traits, Root Reader (Clark et al., 2011) offers mechanisms to measure local traits for individual roots. However, these mechanisms are designed for sparse root networks in which root branches do not occlude each other. We note that neither was optimized for application to field images. Nonetheless, we provide a direct comparison of GiA Roots to our algorithms in the Supplemental Data Set. GiA Roots did not distinguish 128 genotype combinations of the cowpea data set (compare Supplemental Figs. S29 and S30 and Supplemental Data Set S11), whereas our algorithms could distinguish all cowpea genotypes. Recall here that the manually measured traits distinguished all but five genotype combinations. Our image-based trait measurement is a first step toward localized traits under field conditions in the sense that many of our traits are defined with respect to depth and length of the root.

Indeed, measurements of root tip diameters and diameters at 90% depth could not be assessed in a shovelomics setting, but are accessible in gel-based systems of younger roots. The technological possibility to extract root tip information is demonstrated in the example of 10 rice (*Oryza sativa*) genotypes of a previously published study (Iyer-Pascuzzi et al., 2010) in Supplemental Figure S23. These images were previously used for genotype differentiation based on global root traits with the algorithms available in GiaRoots (Galkovskyi et al., 2012). In addition to obvious genotype distinction in many traits, the figure shows that mean tip diameters and the maximal diameter at 90% depth have good differentiation capabilities, when derived with our algorithms. Indeed, many traits can be derived for both settings and may enable translational studies from the field to the laboratory.

The traits extracted with our imaging pipeline may also enhance input to data-driven simulation systems such as SimRoot (Lynch et al., 1997). Such a combination would allow the reconstruction of the complete root system in the future even though the excavation process cuts off some of the root system. The challenge of such data-driven simulation is the relation between traits extracted from images and elementary phenes driving the simulation (York et al., 2013; Postma et al., 2014). Combined model-based and data-supported reconstructions have already been successfully used for tree crowns (Côté et al., 2009). Such a simulation would enable computational experiments of crop root responses to varying environmental conditions such as drought, N, P or K during root growth, even more extensive than known for cauliflower (*Brassica oleracea*; Vansteenkiste et al., 2014).

In summary, our imaging approach and algorithms enable the possibility to phenotype mature root systems under real conditions from objective data. This
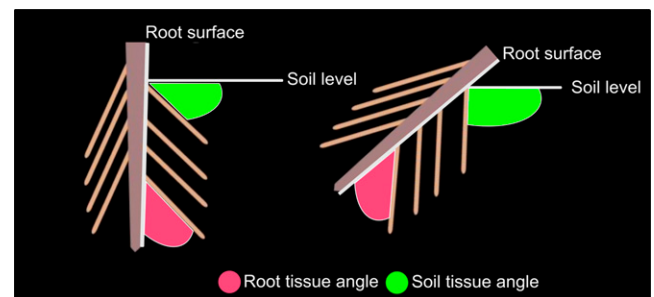

Figure 13. Difference between the RTA (green) and the STA (red). The RTA does not change if the root is rotated on the board. By contrast, the STA on the rotated root on the right is larger than on the left.

approach has addressed an identified need for phenotyping protocols for mature root systems operated in a high-throughput fashion under real soil conditions to extract root architectural traits (Dhondt et al., 2013). We envision future extensions to leverage cloud and grid computing platforms as infrastructure (Moore et al., 2013) to calculate image-based traits from thousands of images in parallel. In this way, field experiments may enhance their statistical power and significance to levels currently achieved in laboratory environments.

MATERIALS AND METHODS

Plant and Growth Conditions

We selected nine maize (*Zea mays*) lines from a planting of a subset of the Wisconsin diversity panel (Hansey et al., 2011) grown for 8 to 12 weeks at the Ukulima Root Biology Center (URBC; Alma, Limpopo Province, South Africa). Five lines (B73, H99, Mo17, OH43, and W64A) were selected as being well-studied lines that are also included in the EUROOT maize panel (http://www.euroot.eu/). Four replicates of each line were planted in an incomplete block design. A further four lines (4226, B103, Tr, and W23) were selected with contrasting RSA, specifically to represent the range of nodal root angles, nodal root numbers, and lateral branching density as shown in Figure 8. These lines were replicated three times. For all of these lines, four root crowns per plot were excavated, and two were scored, resulting in a total of 44 imaged roots and four to six measurements per genotype. Images were taken separately for crown and brace roots, each containing an excised crown root or brace root, respectively, resulting in 88 images in total.

Cowpea (*Vigna unguiculata*) roots were collected in January 2013 at the URBC from a 188-line diversity panel grown for 5 to 6 weeks under nonlimiting conditions. The Supplemental Data contain a list of all genotypes used in this study (CowpeaGenotypeMap.xlsx).

For completeness, we cite the following growth conditions of the rice (*Oryza sativa*) data set given in Iyer-Pascuzzi et al. (2010): "Seeds were dehulled and sterilized with 10% peroxide for 10 min, followed by 70% ethanol for 1 min, and rinsing three times with sterile water. Sterilized seeds were planted at approximately 1 cm below the surface of the gel. Plants were grown in 2 L ungraduated borosilicate cylinders (Fisher) filled with 750 mL Yoshida's nutrient solution (Yoshida et al., 1976) and 0.3% Gelzan (the highest grade of gellan gum available; Sigma). Cylinders are approximately 520 mm high, with an o.d. of 82.5 mm. To prevent the agar from moving during imaging, six to eight glass pipette tips were bonded to the bottom of each cylinder with Sylgard 184 (Robert McKeown Co.). Plants were grown for 14 d at 12-h day/night, 28°C day, 25°C night. Images were taken 14 dap…. Twelve rice (*Oryza sativa*) genotypes were used: 93-11 (9311; *indica*), Caipo (Cai; *tropical japonica*), Basmati 217 (Ba217; *Basmati*), Jefferson (Jef; *tropical japonica*), Teqing (Teqing; *indica*), Lemont (Lemont; *tropical japonica*), Moroberekan (Moro; *tropical japonica*), Nipponbare (Nipp; *temperate japonica*), IR64 (IR64; *indica*), Carolina Gold (Gold; *japonica*), Bala (*indica*), and Azucena (*tropical japonica*). Genotypes were chosen based on parentage of available QTL mapping populations and to represent both of the two major subpopulations of rice (*indica* and *japonica*). Analyses were performed on six to 18 individuals of each genotype."

Low-Cost, Reproducible, and Field-Based Protocol for Imaging Plant Roots

We extend the shovelomics trait estimation procedures described in Trachsel et al. (2011) with a new imaging board and imaging protocol. The new imaging board consists of a black background with diffuse reflectance properties on which a circle of known diameter is freely positioned (Fig. 2A). Optionally, a rectangular marker that encodes the experimental identification of the root crown in a sequence of letters and numbers can be placed on the board. Suitable boards were simple cutting boards, ordinary black cloth, or plastic painted with blackboard coating. These boards are easily cleaned with a brush or damp cloth to remove soil and root fragments from previously imaged roots and are low cost and suitable for fieldwork.

The protocol for imaging with this modified board is as follows. First, the root crown is placed on the board, oriented such that the stem is perpendicular

to the horizontal edge of the board. A predefined number of excised roots (e.g. basal or nodal roots) can be placed on the board. The placement of these elements is arbitrary so long as none of the imaged objects (i.e. circle, marker, root crown, and excised roots) intersects another object (Fig. 2). Including multiple root components on the same image enables downstream analysis of multiple root traits.

Next, images of the root system should be photographed using a digital camera mounted on a tripod (Fig. 3) at about 30 to 50 cm above the imaging board. We used high-end consumer cameras in this study. The known dimensions of the circle correct for tilting of the camera normal to the imaging plane and enable automated correction of the trait estimations. As we describe below, our methods provide mechanisms to deal with irregular ambient light and visual noise that may lead to varied image quality. Nonetheless, we recommend cleaning the imaging board regularly, while maintaining relatively constant diffuse lighting.

Finally, it is worth noting that our image-based phenotyping pipeline is technologically constrained by the use of digital cameras, which rely on the reflection of light from surfaces and therefore cannot resolve large occlusions of the root system. As a consequence, our pipeline relies on the subjective impression of the field phenotyper to select a representative nodal root to detail the fine root structure. Measuring complete mature root architectures would require either automated cutting of the root into its individual organs or field-ready three-dimensional imaging systems such as x-ray systems, neither of which is currently available. Given these limitations, we assumed the maize roots to be symmetric to the shoot main axis if only imaged from one side. This assumption allows that the width-related traits (e.g. median width and D and DS values Table I) and root density estimates are the parameters closest to the ones observed in the field.

The Digital Image Analysis Pipeline

Identifying Distinct Components

The original color image taken from the image board (Figure 2IIIa) is converted into a grayscale image. The conversion uses the weighting from the PAL television system, in which the gray value or chrominance Y is derived as the weighted sum of $Y = 0.30R + 0.59G + 0.11B$, where R, G, and B are the red, green, and blue components of each pixel, respectively. The resulting gray image is segmented into a foreground and background by first estimating a global threshold with the Otsu (1975) method. This thresholding method assumes a bimodal distribution of chrominance values, from which an initial global separation threshold is estimated. The initial threshold value is passed into an adaptive thresholding algorithm that locally refines the global threshold in a user-defined window around each pixel. Here, the scaled threshold is the sum of the global threshold and the variance of a Gaussian distribution used to weight pixels within the thresholding window. If the weighted mean of the thresholding window is greater than the global threshold, then the pixel is classified as foreground. Otherwise, the pixel is classified as background. Note that such scaling influences the measurement slightly, because the root appears slightly thicker in the binary image than in the original. The resulting binary image is a segmentation of objects in the foreground and the background. The segmentation is shown in Figure 2IIIb, where the foreground corresponds to white pixels and the background to black pixels. It is noteworthy that our thresholding reduces the number of user-controlled parameters to one if used with our field-imaging protocol. The only user-controlled parameter is the scale parameter that controls weighing of neighboring pixels. All other parameters can be fixed to standard values in our setup.

To distinguish the objects on the board from noise in the foreground, we first use connected component labeling (Samet, 1981) to identify clusters of neighboring foreground pixels called components. We assume that none of the four placed object classes (Fig. 2III) intersect, and no additional objects are placed on the board. It is a prerequisite that noise pixels do not group into clusters that take up more area than the placed objects. Keeping the board clean from soil artifacts while images are taken can enforce this noise constraint. The root crown is defined as the component containing the largest number of pixels. Circle marker, excised root, and the experimental tag are distinguished using prior knowledge on their likely shape. The circle is detected as the component with a side-length ratio of the bounding box closest to 1 and is distinguished by a foreground percentage of 78%, corresponding to the fraction of area taken up by a circle inscribed into a square. Excised roots are detected as the next set of largest components. They are distinguished by the ratio of foreground to background pixels within the bounding box of the extracted object. We assume that the tag has a higher foreground to

background ratio than the root and should be the second smallest component in terms of overall number of pixels. As a result, we obtain an image mask with a separated foreground and background for each object on the imaging board.

Traits Derived from the Image Mask

The root crown image provides the input to compute the root-width profile as illustrated in Figure 11, root width and depth, as well as root density. The root-width profile is computed per row of the image raster. The root width per row is given as the distance between the first and the last foreground pixels in the row. From the width profile, we calculate so-called D values as the cumulative width at a certain fraction of the maximal depth. For example, D10 and D90 represent the sum of all root widths at rows whose vertical location lies between 0% and 10% and between 0% and 90%, respectively, of the total number of rows in the root crown. Furthermore, each D value has a corresponding DS value that is the slope of the tangent at each D value. Both D and DS values are novel traits in the literature and represent samples of a polynomial as shown in Figure 11. In practice, the latter can be thought of a normalized root-top angle, as is the case for maize. The ratio between foreground pixels and background pixels in a row is the root density per row, which is averaged to yield the overall root density. The measurements computed from the image mask are similar to the manually measured shovelomics in that they quantify the global shape of the RSA in absolute values of the whole root system or at certain depth levels. Traits derived in relation to the maximal depth and/or width in the case of D and DS values are inaccessible in the field. The latter are said to be relative traits, whereas all other traits are absolute traits.

The individual masks of the root crown and the excised root are used to derive estimates of root width, height, density, and angles. Traits are computed on the basis of the extracted root masks for the crown and the excised root with their corresponding RTPs as described in the next section.

Computing RTPs

The previously computed mask images of the root crown and excised roots serve as input to the RTP algorithm. First, we compute the medial axis (Fig. 2IVc) of the root object using morphological hit-and-miss transform (Serra, 1982) with a 3×3 cross mask. The calculation of the medial axis implies knowledge of the distance field (Fig. 2IVb). The distance field defines for each root pixel the shortest Manhattan distance to a nonroot pixel. The medial axis is the collection of points within the root that are equidistant to at least two nonroot pixels; in this way, the medial axis approximates center lines within the segmented root system (Supplemental Fig. 22). Ideally, the medial axis contains all branching points and tips visible on the extracted root image. This would be the case for plant roots that have been separated and placed on a board. Instead, for mature roots imaged in the field, occlusion of single roots leads to loops in the medial axis, which does not correspond to the branching structure of the root system. The RTP approach aims to estimate architectural traits between the computations of the medial axis that may include loops, as extracted from the segmented root image, and the loop-free architecture of plant roots. We define a single RTP as the shortest path along the medial axis from a given root tip to the root top, in which the root top is the location where the root got separated from the shoot (Supplemental Data Set).

The computation of the shortest paths forming the RTP skeleton leverages Dijkstra's shortest path algorithm (Goldberg and Harrelson, 2005) from each tip to the start of the root top along the medial axis. Each pixel belonging to the medial axis is associated with a diameter d_x derived from the previously computed distance field. In the following, we weigh the shortest path calculation with $w_{x1,x2}$ for each step from one medial axis pixel p_1 to an adjacent pixel p_2 as the difference between the maximal stem diameter d_{max} and the average diameter of p_1 and p_2.

$$w_{x1,x2} = d_{max} - \frac{d_{x1} + d_{x2}}{2}$$

All RTPs of a root assemble a skeleton graph represented as a set of image pixels, where pixels with two neighbors are elongated root parts; pixels with three or more neighbors are a branching point where multiple root parts intersect. Pixels with only one neighbor correspond to a root tip or the start of the root stem. The RTP skeleton is weighted by the number of paths as a measure of root thickness at all locations of the skeleton. Underlying the definition of RTPs is the assumption that RTPs to all visible tips in the image approximate the actual root shape well.

The RTP skeleton describes significant root parts by the number of paths passing through the same location in the image. Because RTPs are determined on the basis of detectable tips in the image, a significant root part is either roots with many child roots or larger amounts of adhered roots whose tips are visible in the image. The pseudocode shown in Figure 12 demonstrates a simple procedure to compute RTPs from a medial axis input.

A central path with the largest average diameter is assumed to be the taproot in dicots. Along the central path, branches are counted and measured. For monocots such as maize, a central root is not accessible via the image and the central path only contains information about the start of the root crown, reflected in many paths emerging within a small portion of the central path. Hence, only the fine structure of dense monocot roots such as maize is analyzed with RTPs on an excised root sample.

In our example in Figure 2IId, all paths emerge from the location where the root stem was separated from the shoot. At this location, the number of RTPs equals the number of tips detectable in the image. At every branching point of the RTP skeleton, a certain number of paths split off into another branch, such that the number of paths present after the split is equal to the number of paths in the respective subtree of the branch (Supplemental Fig. 28).

Traits Derived from the RTP Skeleton

The RTP skeleton is a loop-free sampling of the medial axis (Supplemental Fig. S27) derived from the root shape visible in the image. As a consequence, the RTP skeleton allows the calculation of the length of significant root parts, the radius at each location as the distance to one of the at least two closest pixels on the root mask boundary, and branching frequencies and path length from the distance between branching points and angles between a root emerging from the tissue of a parent root. Computing the root length from the point of emergence to the tip requires care. The length from a branching point to a root tip includes the radius at the branching point, because the skeleton is centered within the root. The tip of the skeleton is also a center with respect to the root tissue. Therefore, the radius at the branching point has to be subtracted from the length and the tip radius has to be added. We used a threshold of three pixels to eliminate spurious branches (Fig. 2, IVc and IVd) resulting from boundary disturbances of the foreground mask. Note that this filtering is applied after the detection of the central path. Angles are calculated as the angle between the tangent to the parent root at location of the branching point and the line determined by the least-squares fit through the emerging path. We calculate two different angles: the STA and the RTA. The STA is the angle formed by the fit line and the x axis. Nevertheless, the STA is dependent on the placement of the root on the imaging board as shown in Figure 13, if angular symmetry of root with the stem cannot be assumed.

This dependency on the root placement motivated the development of the RTA. A tangent is estimated as the least-square fit through a definable window size around a branching point on the central path. This angle calculation takes the local curvature of the nodal root into account and is independent from the root placement on the board, because it is locally related to the root.

The spatial root distribution is represented as a vector. The spatial root distribution is calculated as the difference vector between the centers of the bounding box (Supplemental Fig. S26) of the RTP skeleton and the mean coordinate of the RTP skeleton excluding the central path. In the given coordinate system of the image, the x-component of the vector represents the symmetry of the root to the y-axis, which is expected to be useful especially in dicots. The y-component reflects the depth at which the majority of roots are located. Diameter measurements of the central path in predefined intervals relative to the maximal length of the central path can be retrieved on dicots and on excised roots. The distance between branching points along an excised root enables the computation of branching frequency, lateral length, and diameters from the RTPs.

Imaging Specifications

The maize study was performed with a Canon PowerShot A1200 digital camera with a focal length of 6 mm and a maximal aperture of 3.3. The cowpea case study was imaged with a Nikon D70s digital camera using a focal length of 18 mm and a maximal aperture of 3.6. In both case studies, only optical zoom was used to adjust the field of view in all studies, such that an interpolation effect because of software-enhanced resolution could be avoided.

Images for the maize diversity panel were taken at a resolution of 4,000 $\times$ 3,000 pixels. Images for which the scale maker was not extractable were removed from the data set and the comparison.

Except for the brace root images of B73, three to six images of sufficient quality were obtained. Overall, 85 images were used. The scale marker varied in 210.47 pixels in the x direction and 217.22 pixels in the y direction, with SDs of 10.31 and 9.80, respectively. The threshold scale factor for deriving the image mask was 20.0, and we used an 80×80 window for the adaptive thresholding.

The images for the cowpea study were taken at a resolution of 3,008 × 2,000 pixels. From the original 1,500 images taken, we used 1,444 that had sufficient quality, such that six to eight samples per genotype were obtained. The scale marker width is 238.45 pixels in the x direction and 237.79 pixels in the y direction, with SDs of 5.04 and 2.44, respectively. The threshold scale factor for deriving the image mask was 5.0, and we used an 80 × 80 window for the adaptive thresholding.

For completeness, we cite the following imaging setup given in Iyer-Pascuzzi et al. (2010) for the rice data set: "Plants were imaged using a Photo Capture360 turntable and software from Ortery Technologies connected to a Canon PowerShot G7 digital camera and Dell Latitude 620 laptop computer. Cylinders were lit from the sides with fluorescent light bulbs, and from below with a UV light box (VWR); lighting conditions were similar for all experiments. Images from 20 angles per plant per day were acquired. The threshold scale factor for deriving the image mask was 1.0, and we used a 80 × 80 window for the adaptive thresholding." The images to determine the technical error of the imaging protocol were taken with an Olympus SZ-12 camera having a focal length of 4 mm and a maximal aperture of 3.17 on a Sony VCT-R 640 tripod with ground-level adjustment. The images were taken at an original resolution of 4,288 × 3,216 pixels. We cut out the image portion in which the root is visible. The background was painted with Blick Artists Black Gesso paint (1 US FL QT). Five researchers took 10 images of a bean and a maize root crown. All persons were exposed to the imaging procedure for the first time. All 50 images per root were correctly computed.

Online Access to the Data and a Beta Version of the Source Code

We provide access to the data used in this article via an online application at http://www.dirt.biology.gatech.edu. This online tool is a system-specific solution that allows other researchers to access and use the data. The source code for the algorithms is available as a free download on the Web site. The online platform is implemented in PYTHON 2.7 (Van Rossum and Drake, 2009) using the libraries NumPy (Oliphant, 2006) and SciPy (Oliphant, 2007) to derive the statistics, Mahotas (Coelho, 2013) for image processing, and the graph library graph-tools (http://graph-tool.skewed.de). The Web application is implemented in Drupal (Graf, 2006). The source code of our algorithms is available at https://github.com/abucksch.

Supplemental Data

The following materials are available in the online version of this article.

Supplemental Figure S1. Maize trait correlation between the manually scored lateral length and the image-based measured lateral length.

Supplemental Figure S2. Maize trait correlation between the caliper measurement and the image-based measurement of the stem diameter.

Supplemental Figure S3. Correlation between crown root angle and D10 value.

Supplemental Figure S4. Correlation between brace root angle and D10 value.

Supplemental Figure S5. Correlation between crown root number and D20.

Supplemental Figure S6. Correlation between brace root number and D20.

Supplemental Figure S7. Variability of the image-based brace root measurements.

Supplemental Figure S8. Variability of image-based crown root measurements.

Supplemental Figure S9. Variability of the Shovelomics brace root measurements.

Supplemental Figure S10. Variability of the Shovelomics crown root measurements.

Supplemental Figure S11. RPV analysis of the brace root traits for maize.

Supplemental Figure S12. Heritability of maize traits derived from the crown root images.

Supplemental Figure S13. Heritability of maize traits derived from the brace root images.

Supplemental Figure S14. Inter- and intravarietal variation for crown root traits computed from images.

Supplemental Figure S15. Image-based phenotype differentiation: normalized mean trait values of traits derived from brace root images.

Supplemental Figure S16. Inter- and intravarietal variation for Shovelomics crown root traits of the maize diversity panel.

Supplemental Figure S17. Inter- and intravarietal variation for brace root traits computed from images.

Supplemental Figure S18. Image-based trait estimation variability per genotype for the cowpea diversity panel of 188 genotypes.

Supplemental Figure S19. Shovelomics trait estimation variability per genotype for the cowpea diversity panel of 188 genotypes.

Supplemental Figure S20. Heritability of cowpea traits derived from the brace root images.

Supplemental Figure S21. Variability of image-based traits for the cowpea diversity panel consisting of 188 genotypes.

Supplemental Figure S22. Variability of Shovelomics traits for the cowpea diversity panel consisting of 188 genotypes.

Supplemental Figure S23. Normalized mean values of rice genotypes.

Supplemental Figure S24. Monocot root nomenclature on the example of maize.

Supplemental Figure S25. Dicot root nomenclature on the example of bean.

Supplemental Figure S26. The bounding box concept.

Supplemental Figure S27. The medial axis concept.

Supplemental Figure S28. Simplified illustration of the RTP path extraction procedure.

Supplemental Figure S29. Trait variability for the cowpea data set derived with the software GIA Roots.

Supplemental Figure S30. RPV analysis of the GIA Root traits for the cowpea data set.

Supplemental Figure S31. Correlation of stem diameters in cowpea to manually measured stem diameters on a per plant basis of 1,432 individual plants.

Supplemental Figure S32. Correlations between image-based average lateral length and lateral length bins for maize crown roots.

Supplemental Figure S33. Correlation between manual density measures and image-based measures of root density for maize.

Supplemental Figure S34. Correlation between image-based D10 trait and the manually measured maize crown root angle on a per plant basis.

Supplemental Figure S35. Correlation of lateral density scores and lateral branching frequency for excised maize roots.

Supplemental Figure S36. The correlation for the distance to the first lateral for the excised brace roots of maize.

Supplemental Data Set S1. Genotype name to genotype ID map for the cowpea data set.

Supplemental Data Set S2. Image-based trait values for cowpea.

Supplemental Data Set S3. Cowpea Shovelomics.

Supplemental Data Set S4. Cowpea differentiation table for image-based traits.

Supplemental Data Set S5. Cowpea differentiation table for Shovelomics traits.

Supplemental Data Set S6. Image-based trait values for maize.

Supplemental Data Set S7. Maize Shovelomics crown root.

Supplemental Data Set S8. Maize Shovelomics brace root.

Supplemental Data Set S9. Technical error results for bean.

Supplemental Data Set S10. Technical error results for maize.

Supplemental Data Set S11. Differentiation table GIA Roots.

Supplemental Data Set S12. The Python Source Code used in the article.

LITERATURE CITED

Araus JL, Cairns JE (2014) Field high-throughput phenotyping: the new crop breeding frontier. Trends Plant Sci 19: 52–61

Armengaud P, Zambaux K, Hills A, Sulpice R, Pattison RJ, Blatt MR, Amtmann A (2009) EZ-Rhizo: integrated software for the fast and accurate measurement of root system architecture. Plant J 57: 945–956

Band LR, Fozard JA, Godin C, Jensen OE, Pridmore T, Bennett MJ, King JR (2012) Multiscale systems analysis of root growth and development: modeling beyond the network and cellular scales. Plant Cell 24: 3892–3906

Brooks TLD, Miller ND, Spalding EP (2010) Plasticity of Arabidopsis root gravitropism throughout a multidimensional condition space quantified by automated image analysis. Plant Physiol 152: 206–216

Clark RT, MacCurdy RB, Jung JK, Shaff JE, McCouch SR, Aneshansley DJ, Kochian LV (2011) Three-dimensional root phenotyping with a novel imaging and software platform. Plant Physiol 156: 455–465

Coelho LP (2013) Mahotas: Open source software for scriptable computer vision. J Open Res Software 1: e3

Côté JF, Widlowski JL, Fournier RA, Verstraete MM (2009) The structural and radiative consistency of three-dimensional tree reconstructions from terrestrial lidar. Remote Sens Environ 113: 1067–1081

Da Silva D, Boudon F, Godin C, Puech O, Smith C, Sinoquet H (2006) A critical appraisal of the box counting method to assess the fractal dimension of tree crowns. In G Bebis, R Boyle, B Parvin, D Koracin, P Remagnino, A Nefian, G Meenakshisundaram, V Pascucci, J Zara, J Molineros, H Theisel, T Malzbender, eds, Advances in Visual Computing, Vol 4291. Springer, Berlin, pp 751–760

de Dorlodot S, Forster B, Pagès L, Price A, Tuberosa R, Draye X (2007) Root system architecture: opportunities and constraints for genetic improvement of crops. Trends Plant Sci 12: 474–481

Delannay X, McLaren G, Ribaut JM (2012) Fostering molecular breeding in developing countries. Mol Breed 29: 857–873

Den Herder G, Van Isterdael G, Beeckman T, De Smet I (2010) The roots of a new green revolution. Trends Plant Sci 15: 600–607

Dhondt S, Wuyts N, Inzé D (2013) Cell to whole-plant phenotyping: the best is yet to come. Trends Plant Sci 18: 428–439

Downie H, Holden N, Otten W, Spiers AJ, Valentine TA, Dupuy LX (2012) Transparent soil for imaging the rhizosphere. PLoS ONE 7: e44276

Einspahr DW, Van Buijtenen J, Peckham J (1963) Natural variation and heritability in triploid aspen. Silvae Genet 12: 51–58

Fiorani F, Rascher U, Jahnke S, Schurr U (2012) Imaging plants dynamics in heterogenic environments. Curr Opin Biotechnol 23: 227–235

Fitter A (2002) Characteristics and functions of root systems. In U Kafkafi, Y Waisel, A Eshel, eds, Plant Roots: The Hidden Half, Ed 3. CRC Press, Boca Raton, FL, pp 15–32

French A, Ubeda-Tomás S, Holman TJ, Bennett MJ, Pridmore T (2009) High-throughput quantification of root growth using a novel image-analysis tool. Plant Physiol 150: 1784–1795

Furbank R (2009) Plant phenomics: from gene to form and function. Funct Plant Biol 36: v–vi

Galkovskyi T, Mileyko Y, Bucksch A, Moore B, Symonova O, Price CA, Topp CN, Iyer-Pascuzzi AS, Zurek PR, Fang S, et al (2012) GiA Roots: software for the high throughput analysis of plant root system architecture. BMC Plant Biol 12: 116

Gil Y, Deelman E, Ellisman M, Fahringer T, Fox G, Gannon D, Goble C, Livny M, Moreau L, Myers J (2007) Examining the challenges of scientific workflows. IEEE Computer 40: 24–32

Godfray HC, Beddington JR, Crute IR, Haddad L, Lawrence D, Muir JF, Pretty J, Robinson S, Thomas SM, Toulmin C (2010) Food security: the challenge of feeding 9 billion people. Science 327: 812–818

Goldberg AV, Harrelson C (2005) Computing the shortest path: a search meets graph theory. In Proceedings of the Sixteenth Annual ACM-SIAM Symposium on Discrete Algorithms. Society for Industrial and Applied Mathematics, Philadelphia, pp 156–165

Graf H (2006) Drupal. Addison-Wesley, Munich

Gregory PJ, Bengough AG, Grinev D, Schmidt S, Thomas WBT, Wojciechowski T, Young IM (2009) Root phenomics of crops: opportunities and challenges. Funct Plant Biol 36: 922–929

Gregory PJ, George TS (2011) Feeding nine billion: the challenge to sustainable crop production. J Exp Bot 62: 5233–5239

Hansey CN, Johnson JM, Sekhon RS, Kaeppler SM, de Leon N (2011) Genetic diversity of a maize association population with restricted phenology. Crop Sci 51: 704–715

Hargreaves CE, Gregory PJ, Bengough AG (2009) Measuring root traits in barley (Hordeum vulgare ssp. vulgare and ssp. spontaneum) seedlings using gel chambers, soil sacs and X-ray microtomography. Plant Soil 316: 285–297

Hochholdinger F (2009) The maize root system: morphology, anatomy, and genetics. In Handbook of Maize: Its Biology. Springer, New York, pp 145–160

Intergovernmental Panel on Climate Change (2014) Contribution of Working Group I to the Fifth Assessment Report of the Intergovernmental Panel on Climate Change. In TF Stocker, D Qin, GK Plattner, MMB Tignor, SK Allen, J Boschung, A Nauels, Y Xia, V Bex, PM Midgley, eds, Climate Change 2013: The Physical Science Basis. Cambridge University Press, New York, p 1535

Iyer-Pascuzzi AS, Symonova O, Mileyko Y, Hao Y, Belcher H, Harer J, Weitz JS, Benfey PN (2010) Imaging and analysis platform for automatic phenotyping and trait ranking of plant root systems. Plant Physiol 152: 1148–1157

Le Bot J, Serra V, Fabre J, Draye X, Adamowicz S, Pagès L (2010) DART: a software to analyse root system architecture and development from captured images. Plant Soil 326: 261–273

Lobet G, Draye X, Périlleux C (2013) An online database for plant image analysis software tools. Plant Methods 9: 38

Lobet G, Pagès L, Draye X (2011) A novel image-analysis toolbox enabling quantitative analysis of root system architecture. Plant Physiol 157: 29–39

Lynch J (1995) Root architecture and plant productivity. Plant Physiol 109: 7–13

Lynch JP (2007) Turner review no. 14. Roots of the second green revolution. Aust J Bot 55: 493–512

Lynch JP (2013) Steep, cheap and deep: an ideotype to optimize water and N acquisition by maize root systems. Ann Bot (Lond) 112: 347–357

Lynch JP (2011) Root phenes for enhanced soil exploration and phosphorus acquisition: tools for future crops. Plant Physiol 156: 1041–1049

Lynch JP, Nielsen KL, Davis RD, Jablokow AG (1997) SimRoot: modelling and visualization of root systems. Plant Soil 188: 139–151

Mairhofer S, Zappala S, Tracy S, Sturrock C, Bennett MJ, Mooney SJ, Pridmore TP (2013) Recovering complete plant root system architectures from soil via x-ray μ-computed tomography. Plant Methods 9: 8

Mairhofer S, Zappala S, Tracy SR, Sturrock C, Bennett M, Mooney SJ, Pridmore T (2012) RooTrak: automated recovery of three-dimensional plant root architecture in soil from x-ray microcomputed tomography images using visual tracking. Plant Physiol 158: 561–569

Maronna RA, Martin RD, Yohai VJ (2006) Robust Statistics: Theory and Methods. John Wiley and Sons, Ltd, Chichester, UK

Mooney SJ, Pridmore TP, Helliwell J, Bennett MJ (2012) Developing x-ray computed tomography to non-invasively image 3-D root systems architecture in soil. Plant Soil 352: 1–22

Moore CR, Johnson LS, Kwak IY, Livny M, Broman KW, Spalding EP (2013) High-throughput computer vision introduces the time axis to a quantitative trait map of a plant growth response. Genetics 195: 1077–1086

Naeem A, French AP, Wells DM, Pridmore TP (2011) High-throughput feature counting and measurement of roots. Bioinformatics 27: 1337–1338

Nelson WJ, Lee BC, Gasperini FA, Hair DM (2012) Meeting the challenge of feeding 9 billion people safely and securely. J Agromed 17: 347–350

Nielsen KL, Lynch JP, Weiss HN (1997) Fractal geometry of bean root systems: correlations between spatial and fractal dimension. Am J Bot 84: 26–33

Nielsen KL, Miller CR, Beck D, Lynch JP (1999) Fractal geometry of root systems: field observations of contrasting genotypes of common bean (Phaseolus vulgaris L.) grown under different phosphorus regimes. Plant Soil **206**: 181–190

Oliphant TE (2006) A Guide to NumPy, Vol 1. USA: Trelgol Publishing

Oliphant TE (2007) Python for Scientific Computing. Comput Sci Eng **9**: 10–20

Otsu N (1975) A threshold selection method from gray-level histograms. Automatica **11**: 23–27

Pieruschka R, Poorter H (2012) Phenotyping plants: genes, phenes and machines. Funct Plant Biol **39**: 813–820

Postma JA, Schurr U, Fiorani F (2014) Dynamic root growth and architecture responses to limiting nutrient availability: linking physiological models and experimentation. Biotechnol Adv **32**: 53–65

Pound MP, French AP, Atkinson JA, Wells DM, Bennett MJ, Pridmore T (2013) RootNav: navigating images of complex root architectures. Plant Physiol **162**: 1802–1814

Rich SM, Watt M (2013) Soil conditions and cereal root system architecture: review and considerations for linking Darwin and Weaver. J Exp Bot **64**: 1193–1208

Samet H (1981) Connected component labeling using quadtrees. J Assoc Comput Mach **28**: 487–501

Schulz H, Postma JA, van Dusschoten D, Scharr H, Behnke S (2013) Plant root system analysis from MRI images. *In* Computer Vision, Imaging and Computer Graphics: Theory and Application. Springer, Berlin, pp 411–425

Serra J (1982) Image analysis and mathematical morphology. Academic Press, London

Shi L, Shi T, Broadley MR, White PJ, Long Y, Meng J, Xu F, Hammond JP (2013) High-throughput root phenotyping screens identify genetic loci associated with root architectural traits in Brassica napus under contrasting phosphate availabilities. Ann Bot (Lond) **112**: 381–389

Sozzani R, Busch W, Spalding EP, Benfey PN (2014) Advanced imaging techniques for the study of plant growth and development. Trends Plant Sci **19**: 304–310

Spalding EP, Miller ND (2013) Image analysis is driving a renaissance in growth measurement. Curr Opin Plant Biol **16**: 100–104

Tatsumi J, Yamauchi A, Kono Y (1989) Fractal analysis of plant root systems. Ann Bot **64**: 499–503

Topp CN, Iyer-Pascuzzi AS, Anderson JT, Lee CR, Zurek PR, Symonova O, Zheng Y, Bucksch A, Mileyko Y, Galkovskyi T, et al (2013) 3D phenotyping and quantitative trait locus mapping identify core regions of the rice genome controlling root architecture. Proc Natl Acad Sci USA **110**: E1695–E1704

Trachsel S, Kaeppler S, Brown K, Lynch J (2011) Shovelomics: high throughput phenotyping of maize (Zea mays L.) root architecture in the field. Plant Soil **341**: 75–87

Van Rossum G, Drake FL (2009) PYTHON 2.6 Reference Manual. Python Software Foundation, Beaverton, OR

Vansteenkiste J, Van Loon J, Garré S, Pagès L, Schrevens E, Diels J (2014) Estimating the parameters of a 3-D root distribution function from root observations with the trench profile method: case study with simulated and field-observed root data. Plant Soil **375**: 75–88

Wojciechowski T, Gooding MJ, Ramsay L, Gregory PJ (2009) The effects of dwarfing genes on seedling root growth of wheat. J Exp Bot **60**: 2565–2573

York LM, Nord EA, Lynch JP (2013) Integration of root phenes for soil resource acquisition. Front Plant Sci **4**: 355

Yoshida S, Forno DA, Cock JH, Gomez KA (1976) Laboratory Manual for Physiological Studies of Rice. International Rice Research Institute, Los Banos, Laguna, Philippines

Zeng G, Birchfield ST, Wells CE (2008) Automatic discrimination of fine roots in minirhizotron images. New Phytol **177**: 549–557

Zhong D, Novais J, Grift T, Bohn M, Han J (2009) Maize root complexity analysis using a support vector machine method. Comput Electron Agric **69**: 46–50

Zhu J, Ingram PA, Benfey PN, Elich T (2011) From lab to field, new approaches to phenotyping root system architecture. Curr Opin Plant Biol **14**: 310–317